Computation-guided optimization of split protein systems

Taylor B. Dolberg[1,2,9], Anthony T. Meger[3,4,9], Jonathan D. Boucher[2,5], William K. Corcoran[2,5], Elizabeth E. Schauer[1,2], Alexis N. Prybutok[1,2], Srivatsan Raman[3,4,8*], Joshua N. Leonard[1,2,5,6,7*]

[1]Department of Chemical and Biological Engineering, Northwestern University, Evanston, Illinois 60208, United States

[2]Center for Synthetic Biology, Northwestern University, Evanston, Illinois 60208, United States

[3]Department of Biochemistry, University of Wisconsin-Madison, Madison, Wisconsin 53706, United States

[4]Great Lakes Bioenergy Research Center, University of Wisconsin-Madison, Madison, Wisconsin 53706, United States

[5]Interdisciplinary Biological Sciences Program, Northwestern University, Evanston, Illinois 60208, United States

[6]Chemistry of Life Processes Institute, Northwestern University, Evanston, Illinois 60208, United States

[7]Member, Robert H. Lurie Comprehensive Cancer Center, Northwestern University, Evanston, Illinois 60208, United States

[8]Department of Bacteriology, University of Wisconsin-Madison, Madison, Wisconsin 53706, United States

[9]These authors contributed equally to this work

Contact Information

*Corresponding authors: Srivatsan Raman (sraman4@wisc.edu) and Joshua N. Leonard (j-leonard@northwestern.edu)

ABSTRACT

Splitting bioactive proteins, such as enzymes or fluorescent reporters, into conditionally reconstituting fragments is a powerful strategy for building tools to study and control biochemical systems. However, split proteins often exhibit a high propensity to reconstitute even in the absence of the conditional trigger, which limits their utility. Current approaches for tuning reconstitution propensity are laborious, context-specific, or often ineffective. Here, we report a computational design-driven strategy that is grounded in fundamental protein biophysics and which guides the experimental evaluation of a focused, sparse set of mutants—which vary in the degree of interfacial destabilization while preserving features such as stability and catalytic activity—to identify an optimal functional window. We validate our method by solving two distinct split protein design challenges, generating both broad insights and new technology platforms. This method will streamline the generation and use of split protein systems for diverse applications.

KEYWORDS: synthetic biology, split proteins, computational protein design, protein engineering

INTRODUCTION

Split proteins and conditional reconstitution systems are powerful tools for interrogating biology and controlling cell behavior.[1-4] These systems work by splitting a protein into two fragments to disrupt the protein's function. Each fragment is then fused to a partner domain such that the split protein is reconstituted, and its function is restored only when the partner domains interact. This modular strategy may be applied to diverse functional proteins to control bioluminescence[5, 6], fluorescence[7], proteolytic cleavage[8-10] and transcription[11, 12]. As a result, conditionally-reconstituted split proteins have been employed in a variety of applications including probing and discovering new protein-protein interactions[13-16], studying post-translational modifications[17], imposing small molecule-regulated control over enzymatic activity[18, 19], and rewiring cellular signaling[9, 20].

Despite their utility in certain contexts, broader application of split protein systems is largely limited by the spontaneous reconstitution of fragments, resulting in high background activity (**Fig. 1a**). Splitting a protein tends to expose its hydrophobic core, creating highly unfavorable interactions between the core and solvent. Reconstitution is driven by a strong inherent preference to desolvate by recombining the fragments. Evaluating alternative splitting sites can vary reconstitution propensity, but this approach often only partially ameliorates the problem because changing splitting sites may not significantly affect underlying hydrophobic forces. Therefore, it is necessary to identify variants with a reconstitution propensity that precludes spontaneous reconstitution but enables reconstitution under desired conditions. Variants with a range of reconstitution propensities can be generated by random mutagenesis and screened for the desired property. However, high-throughput screening is not readily available for all split protein systems, and low-throughput clonal testing of variants can be laborious and suffer from inefficient exploration of sequence space. Even when screens generate improved variants, it may be difficult to interpret why only certain mutants were successful, and as a result, generalizable rules cannot be transferred to guide the tuning of new split protein systems. Furthermore, split protein systems tuned by mutagenesis exhibit performance characteristics determined by (and limited to) the conditions used in the initial screens, again posing a barrier to general applications.

Here, we report a general strategy based on fundamental principles of protein biophysics for optimizing split protein systems which we term **S**plit **P**rotein **O**ptimization by **R**econstitution **T**uning, or SPORT. We use computational mutagenesis with the Rosetta macromolecular modeling suite to guide limited experimental screening and thereby discretely map the sequence-energy landscape of the split interface. This allows us to determine optimal interaction energies that maximize the performance of the split protein system. We demonstrate proof-of-concept by optimizing a split protease system for conditional reconstitution in two different contexts: membrane-embedded and cytosolic. Our approach generates simple design rules that may be extended to tune other split protein systems for distinct design goals and can be implemented by most research laboratories. This work demonstrates a new method for efficiently engineering split protein systems, which will streamline the generation and expand the use of split protein systems for diverse applications.

RESULTS

Formulation of the design challenge and strategy

As a first step toward developing a strategy that addresses the challenge of designing split proteins, we selected a model system based on the well-studied Tobacco Etch Virus protease (TEVp)—we sought to tune the reconstitution propensity of split TEVp. For this purpose, we modified a synthetic receptor system that we previously reported (Modular Extracellular Split Architecture, or MESA)[21] to serve as a reporter of conditional split TEVp reconstitution. In this testbed, ligand binding-induced dimerization of a membrane receptor reconstitutes an intracellular split TEVp, which then autolytically liberates a sequestered transcription factor to drive reporter gene expression (**Fig. 1b**). Our initial evaluation demonstrated that the canonical split TEVp (split between residues 118/119)[22] showed high propensity to reconstitute, resulting in high background from ligand-independent signaling (**Supplementary Fig. 1**). As the original screens used to identify this split were performed in a soluble rather than membrane-bound context, these data suggest that tethering split TEVp to a membrane may promote reconstitution. Furthermore, we determined

that this problem is not limited to the canonical split site, as other TEVp partitioning also yielded poor performance (**Supplementary Fig. 2**). Given these observations, we formulated a design goal: rationally mutate split TEVp to optimize two key MESA performance characteristics—minimal reporter gene expression in the absence of ligand and a substantial fold increase in reporter expression upon ligand addition.

Biophysical principles underlying SPORT

We developed SPORT, a computation-guided workflow to rationally design split protein interfaces to optimize reconstitution propensity (**Fig. 1c**). SPORT employs Rosetta, a state-of-the-art software package for protein design.[23] Given a protein with a predetermined split site, our first step was to identify key interfacial residues to target for mutagenesis. Residues with large differences in solvent-accessible surface area (SASA)—when comparing intact protein and split fragments—were classified as buried residues. These buried residues are ideal targets for mutagenesis as they likely contribute substantially to the driving force for spontaneous reconstitution. For each buried residue, we performed a comprehensive, *in silico* mutational scan to evaluate the energy perturbation of all possible single-point mutations on the interaction energy across the split protein interface ($\Delta\Delta G_{Interfacial}$) and total stability of the mutated protein ($\Delta\Delta G_{Total}$) relative to the parent. The degree of disruption is a critical design consideration. Insufficient disruption may retain high background activity while excessive disruption may impair catalytic activity due to loss of overall protein stability. Therefore, the interface must be carefully tuned so that the driving force provided by ligand binding-induced dimerization promotes reconstitution. This “Goldilocks zone” likely differs for each individual protein and perhaps depends upon context, and this zone is difficult to define *a priori*. Therefore, our strategy was to identify the Goldilocks zone for a given protein by choosing mutations that span the range of $\Delta\Delta G$ values. We hypothesized that a limited test set of mutants would direct subsequent mutagenesis efforts by predicting desirable mutant combinations from a vast amount of sequence space. Each of these propositions was tested using experimental case studies.

Validating SPORT by tuning a membrane-tethered split TEV protease

123

124 To investigate and validate SPORT, we applied our design workflow to the split TEVp MESA system. We
125 first assessed the per-residue change in solvent accessible surface area (ΔSASA) between the intact form
126 and split fragments (**Fig. 2a**). In total, 130 of the 218 residues showed increased SASA in the isolated
127 fragments. We excluded from this set the catalytic triad and 27 residues lying within a 6 Å coordination
128 sphere around the catalytic triad to avoid perturbing the catalytic function of reconstituted TEVp. Of the
129 remaining 100 positions, we chose the 15 positions with the largest ΔSASA (9 in N-terminal and 6 in C-
130 terminal halves of split TEVp) as candidates for mutagenesis. Next, we evaluated the energy perturbation
131 of all possible single-point mutations (285 in total) at these positions using Rosetta. As expected, few
132 mutations were predicted to increase stability, and a vast majority were destabilizing (**Fig. 2b,**
133 **Supplementary Figure 3**). Many positions exhibited a variety of stabilizing, benign, and destabilizing point
134 mutations that were consistent with structure. For instance, bulky sidechain substitutions (W, F, Y, R, K and
135 H) at position 103 resulted in many steric clashes with neighboring residues (**Fig. 2b** right panel) and
136 subsequently conferred large decreases in predicted stability.

137

138 Guided by these predictions, we next experimentally characterized 20 single-mutant split TEV variants that
139 span a wide range of $\Delta\Delta G_{Interfacial}$ (3.1 to 16.1 Rosetta Energy Units, or REU) and $\Delta\Delta G_{Total}$ (-1.9 to 30 REU)
140 energies (**Fig. 2c**). We observed high background signaling (i.e., reporter expression) for disruptions up to
141 $\Delta\Delta G_{Interfacial}$ ~6.6 REU, which suggested that destabilization was insufficient. However, four out of ten
142 variants with $\Delta\Delta G_{Interfacial}$ >10 REU exhibited reduced background signaling and substantial ligand-induced
143 activation (**Fig. 2c**). The remaining six were completely inactive (or "dead"); they induced no signaling under
144 any conditions. Energy-based partitioning across different phenotypes (inducible, not inducible, and dead)
145 became evident when comparing $\Delta\Delta G_{Interfacial}$ and $\Delta\Delta G_{Total}$ of all 20 single mutant split TEV variants (**Fig.**
146 **2d**). Variants with high background activity due to insufficient destabilization fell in the region where
147 $\Delta\Delta G_{Interfacial}$ < 10 and $\Delta\Delta G_{Total}$ < 10 REU. Variants with the dead phenotype had $\Delta\Delta G_{Interfacial}$ > 10 and
148 $\Delta\Delta G_{Total}$ > 10 REU; since these mutants were expressed, as confirmed by Western blot (**Supplementary**
149 **Fig. 4**), the lack of signaling suggested that these mutations directly preclude reconstitution. Most of the
150 inducible variants (three out of four) were observed in the energy window where $\Delta\Delta G_{Interfacial}$ > 10 and

151 $\Delta\Delta G_{Total}$ < 10 REU, which may represent the Goldilocks zone we hypothesized to exist. An additional region
152 contained a mixture of inducible and dead phenotypes. By inspection of these results, we then proposed a
153 model for broadly classifying experimental phenotypes based on energy partitions (**Fig. 2e**).
154
155 **SPORT predicts outcomes of combining mutations**
156
157 We next evaluated whether our proposed classifier model—developed based upon observations with single
158 mutants—could predict the phenotypes of combined NTEVp and CTEVp mutations, including both double
159 (two mutations on one chain) and paired (one mutation on each chain) mutants derived by combining the
160 initial 14 single non-dead mutations tested (**Fig. 3a**). Of the 67 possible double and paired mutants tested,
161 28 were predicted to be inducible. We experimentally tested 14 of these and found that 10 exhibited
162 inducible signaling as predicted, one was dead, and three were not inducible; this yields an observed
163 accuracy of 0.71 for inducible predictions (**Fig. 3b,c**). Interestingly, three of the prediction failures fell at the
164 low end of the range of predicted changes in interfacial energy, suggesting potential opportunities for
165 refining the classifier model. We also noted an interesting trend in our ΔΔG (total and interfacial)
166 calculations—for the sixty-seven mutants tested, the calculated ΔΔG for the double and paired mutants
167 were nearly identical to the sums of the ΔΔG calculated for the associated single mutants (**Supplementary**
168 **Fig. 5**). Thus, for subsequent analyses of combined mutants, we simply added the effects of single mutants
169 in our calculations.
170
171 We next investigated how variations in expression level might impact the inducibility of the mutants. We
172 used Western blot analysis to normalize and vary chain expression levels by adjusting DNA doses
173 (**Supplementary Fig. 6**). Notably, these constructs remained inducible across the entire range of
174 expression levels tested, suggesting that the biophysical mechanism of optimized split protein reconstitution
175 is robust to variations in the expression levels and ratio of the membrane-bound split TEVp fragments.
176 However, we observed that the performance of these constructs (i.e., fold induction of signaling upon ligand
177 addition) could be substantially improved through tuning expression such that protein levels of each
178 fragment are comparable (**Fig. 3d, Supplementary Fig. 7**). Taken together, these results suggest that a

179 classifier calibrated with a limited set of experimental observations spanning the full range of ΔΔG can
180 predict function of new mutants with high accuracy in a manner that is independent of expression level of
181 the construct.
182
183 **SPORT predicts phenotypes of novel mutations and combinations**
184
185 All mutations previously tested were derived from predictions based on our computational method. Next,
186 we wanted to test a broad set of mutants (outside the calibration set) to investigate the accuracy of our
187 classification scheme. Therefore, we experimentally characterized additional single mutants (not included
188 in the original calibration set) and all combinations of paired mutations derived from both the original and
189 this expanded mutation set (omitting dead constructs); mutants were selected to explore the boundaries of
190 the energy landscape classifier model and were expected to reflect a wide range of induced and uninduced
191 reporter expression levels and ratios (**Figs. 2e**, **3a**). We also sought to investigate whether the phenotypic
192 partitioning demonstrated for inducibility (**Fig. 3b,c**) is extensible to the other phenotype classes (i.e., dead
193 and not inducible). This expanded set paired 10 N-terminal mutations with 16 C-terminal mutations. In
194 general, we observed that variants with larger $\Delta\Delta G_{Interfacial}$ energies had lower reporter expression levels in
195 both the background (OFF) and ligand-induced (ON) states (**Fig. 4a**, left and middle panels). Thus, the cost
196 of lowering the OFF state is to also lower the ON state, but these reductions are not always proportional.
197 This is evident by the diversity of calculated fold inductions (**Fig. 4a**, right panel). Only one variant,
198 H75P/W198E, exhibited a significant decrease in the OFF state and an increase in the ON state relative to
199 wild type (WT). However, the variants with highest fold inductions, such as H75S/I163P (17.3 fold induction)
200 and H75T/I163P (9.92 fold induction), exhibited significantly lower OFF and ON states than did the WT,
201 reflecting a tradeoff between desirable performance characteristics. Overall, we observed moderate
202 agreement between the actual and predicted phenotypes for these novel variants and combinations (**Fig.**
203 **4b**). The classifier model was most accurate for predicting the not inducible phenotype (25 of 29, 86%).
204 Many inducible phenotype predictions were also confirmed (31 of 52, 60%). This success rate is impressive
205 given that phenotypic classification boundaries were set roughly based upon the sparse calibration set (**Fig.**

206 **2e**). Interestingly, this analysis also indicates that the energy landscape calculated by SPORT correlates
207 with each phenotype to differing degrees.
208
209 In order to gain additional insight into how choice of calibration set and sample size may impact the accuracy
210 of SPORT predictions, we performed retrospective bootstrapping analysis of the data presented in **Figure**
211 **4** (see **Supplementary Note 2** for full details). Experimental data were stratified by the energy landscape
212 and partitioned randomly into calibration and prediction subsets. Logistic regression modeling was applied
213 to evaluate the accuracy of classification under various conditions (**Supplementary Fig. 8**). We observed
214 robust prediction accuracy using multiple unique calibration sets and using sample sizes ranging from 4 to
215 28. This outcome suggests that our ability to generate a general classification model was not dependent
216 upon the specific calibration data we used in our initial characterization experiment (**Fig. 2**), and that a
217 relatively small set of calibration data drawn from a distribution like that included in **Figure 4** would be
218 sufficient to generate a general classification model.
219
220 **Extension of SPORT predictions to new design goals**
221
222 A major limitation to current approaches for employing split proteins is that often a variant selected to
223 perform well in one context fails in a different context. To investigate whether the SPORT design method is
224 generalizable beyond our initial model system, we developed a distinct model system. This new system
225 employs split TEVp in a soluble form, where we hypothesized that a different reconstitution propensity
226 would be required compared to the membrane-bound model system. To generate such a soluble test
227 system (**Fig. 5a**), ligand binding domains were fused to split TEVp domains along with a soluble
228 transcription factor flanked by protease cleavage sites and nuclear export signals (NES); thus, TEVp-
229 mediated cleavage removes the NES from the transcription factor to enable nuclear localization and
230 reporter expression. We first developed and tested a panel of soluble transcription factors that could
231 implement this mechanism. This evaluation included varying the number of NES elements, their placement
232 at N and/or C terminus of the transcription factor, and the P1' residue of the TEVp cleavage sequence
233 which governs cleavage kinetics[24] (**Fig. 5b**). Several soluble transcription factor constructs exhibited the

234 desired phenotype of low signaling in the absence of TEVp and high signaling when co-expressed with full
235 TEVp; construct TF10 was selected for evaluating split TEVp variants.
236
237 Using our soluble split TEVp test system, we evaluated a panel of 10 single TEVp mutants and 10 paired
238 TEVp mutants spanning a range of interfacial energies **(Fig. 5c**). The construct based upon WT split TEVp
239 exhibited a substantial fold induction, which is consistent with the fact that this split protein was identified
240 by screens performed in the soluble phase[22]. However, the WT construct also yielded high background
241 signaling in the absence of ligand, indicating an opportunity to improve performance. For modest increases
242 in $\Delta\Delta G_{Interfacial}$ (~0–3.6 REU), background signaling persisted. For intermediate increases in $\Delta\Delta G_{Interfacial}$ (~6-
243 10 REU), a mixture of phenotypes was observed, including dead constructs and those with both
244 substantially reduced background signaling and substantial fold inductions. For large increase in
245 $\Delta\Delta G_{Interfacial}$ > ~10 REU, constructs were generally weakly-inducible or dead. Thus, a focused evaluation of
246 20 design variants, guided by SPORT, yielded ~5 variants exhibiting improved performance compared to
247 the WT construct. Altogether, these observations demonstrate that the SPORT method and associated
248 energy landscape concept can be employed to efficiently solve distinct split protein optimization challenges.
249
250 **DISCUSSION**
251
252 In this study, we developed and validated what is—to our knowledge—the first computational strategy for
253 tuning split protein reconstitution propensity. Although the split TEVp MESA used as our first model system
254 would have been deemed infeasible using standard evaluations of split proteins (**Supplementary Figs. 1-**
255 **2**), application of SPORT to tune this system yielded multiple high-performing new synthetic receptor
256 scaffolds (**Fig. 3d**). We show that unlike the classical MESA receptors we have characterized in prior work[21,
257 25, 26], split TEVp MESA tuned by SPORT exhibit excellent performance characteristics (i.e., low-background
258 and high fold-induction) in a manner that is robust to variations in both biosensor expression level and the
259 ratio at which biosensor chains are expressed (**Supplementary Figure 7)**. This property is of great practical
260 utility, as it precludes the need to carefully tune the implementation of each biosensor.
261

Several important insights emerged from this study. First, our approach demonstrated that testing a sparse set of mutants along the energy landscape is an effective strategy to choose optimal interfacial energies to promote conditional reconstitution. Second, multiple point mutations with similar energies exhibited similar performance, which suggests reconstitution propensity depends on the energy of destabilization but is agnostic to specific mutations. Third, the concept of a Goldilocks zone is likely generalizable to different proteins and application contexts, but the optimal energy window may have to be adjusted on a case-by-case basis. We find that membrane-bound split proteins must be destabilized to a greater degree than soluble split proteins in order to avoid spontaneous reconstitution. Altogether, these results show that split protein systems can be engineered based on fundamental principles of protein biophysics, which obviates the need for exhaustive screening and generates rules applicable to new candidate proteins.

There are several interesting opportunities for extending and improving SPORT in future work. First, although our analysis showed that SPORT can be used to identify mutations that confer specific energy changes, it does not yet enable *a priori* prediction of where the Goldilocks zone will fall for new applications. It is possible that subsequent analysis of many case studies could identify trends that enable such predictions and thus harness SPORT to further focus experimental investigations. An additional opportunity is pairing SPORT with a multiparameteric optimization framework for exploring pareto-optimal tradeoffs between performance characteristics; for example, in our model system, there seems to be such a tradeoff between low background in the ligand-free state and high signaling in the ligand-induced state. Finally, the SPORT algorithm itself may be refined to better avoid false positives (e.g., dead mutants that share a region of the energy landscape with inducible variants). Altogether, our findings suggest many opportunities for expanding the utility of split proteins for many new applications and highlight the impact of SPORT-guided development of novel biochemical and synthetic biology tools.

METHODS

General DNA assembly

290 Plasmid cloning was performed using standard molecular biology techniques of PCR and restriction
291 enzyme cloning with Phusion DNA Polymerase (NEB), restriction enzymes (NEB; Thermo Fisher), T4 DNA
292 Ligase (NEB), and Antarctic Phosphatase (NEB). Development of the tTA-responsive YFP reporter plasmid
293 was described previously[21]. Plasmids were transformed into chemically competent TOP10 *E. coli* (Thermo
294 Fisher) and grown at 37˚C. Plasmid maps are provided as GenBank files (**Supplementary Data 1**).
295
296 **Plasmid preparation**
297 Plasmid DNA used for transfection was prepared using the PEG precipitation method, which was previously
298 described in detail.[27]
299
300 **Cell culture**
301 HEK293FT cells (Life Technologies/Thermo) were maintained at 37°C incubator and 5% CO_2. Cells were
302 cultured in DMEM (Gibco 31600-091) with 10% FBS, 6 mM L-glutamine (2 mM from Gibco 31600-091 and
303 4 mM from additional Gibco 25030-081), penicillin (100 U/µL), and streptomycin (100 µg/mL) (Gibco
304 15140122).
305
306 **Transfection**
307 Transfections were performed in 24 well plates seeded at 1.5 x 10^5 cell in 0.5 mL of DMEM media. At 6-8
308 hours post-seeding, cells were transfected using calcium phosphate method with a total DNA content of 1-
309 2 ug DNA per mL of media, using DNA prepared by PEG precipitation. All experiments included blue
310 fluorescent protein (BFP) as a control to assess transfection efficiency. The exact DNA amounts added to
311 the mix per well are as follows, unless otherwise stated in figure captions: 25 ng of each TEVp chain, 200
312 ng of BFP control, 200 ng of YFP reporter plasmid, and 150 ng of pcDNA plasmid. This mixture was added
313 dropwise to an equal-volume solution of 2x HEPES-Buffered Saline (280 mM NaCl, 0.5 M HEPES, 1.5 mM
314 Na_2HPO_4) and gently pipetted up and down four times. After 2.5 minutes, the solution was mixed vigorously
315 by pipetting ten times and 100 µL of this mixture was added dropwise to each well of the plated cells, and
316 the plates were swirled gently. For functional experiments, 12 hours post-transfection, media containing 0.1
317 µM rapamycin analog (Takara AP21967) or 0.1% ethanol as a control was added to cells. At 24-30 hours

318 post-media change, cells were harvested for flow cytometry with Trypsin-EDTA, which was then quenched
319 with medium, and the resulting cell solution was added to at least 2 volumes of FACS buffer (PBS pH 7.4
320 with 2–5 mM EDTA and 0.1% BSA). Cells were spun at 150 x g for 5 min, FACS buffer was decanted, and
321 fresh FACS buffer was added. All experiments were performed in biological triplicate.
322
323 **Flow Cytometry**
324 Approximately 10^4 live cells from each transfected well of the 24-well plate were analyzed using a BD LSR
325 Fortessa Special Order Research Product (Robert H. Lurie Cancer Center Flow Cytometry Core) running
326 FACSDiva software. Samples were analyzed using FlowJo v10 software (FlowJo, LLC). The HEK293FT
327 cell population was identified by FSC-A vs. SSC-A gating, and singlets were identified by FSC-A vs. FSC-
328 H gating. A control sample of cells—generated by transfecting cells with a mass of pcDNA (empty vector)
329 equivalent to the mass of DNA used in other samples in the experiment—was used to distinguish
330 transfected and non-transfected cells. For the single-cell subpopulation of the pcDNA-only sample, a gate
331 was made to identify cells that were positive for the constitutively driven blue fluorescent protein (BFP) used
332 as a transfection control in other samples such that the gate included no more than 1% of the non-
333 fluorescent cells. The mean fluorescence intensity (MFI) of the single-cell transfected population was
334 calculated and exported for further analysis. BD LSR Fortessa settings used were as follows: BFP was
335 collected in the Pacific Blue channel (405 nm excitation, 450/50 nm filer) and EYFP was collected in the
336 FITC channel (488 nm excitation, 505 LP and 530/30 nm filter). To quantify reporter expression, the FITC
337 channel MFI was averaged across three biological replicates. Cell autofluorescence was subtracted and
338 MFI was converted to Mean Equivalents of Fluorescein (MEFLs) using the coefficient determined by the
339 calibration curve of UltraRainbow Calibration Particles (Spherotech URCP-100-2H) run in each individual
340 experiment. Standard error was propagated through all calculations.
341
342 **Western Blotting**
343 Western blots were performed to evaluate protein expression and normalize total expression of each TEVp
344 chain. A 3X-FLAG tagged NanoLuciferase as a normalization control, and images were analyzed using
345 ImageJ software. A detailed western blot protocol was previously described.[27]

346

347 **Solvent-accessible Surface Area**

348 The structure of TEVp was obtained from the Research Crystallography for Structural Bioinformatics
349 (RCSB) PDB (ID code: 1LVM). Per-residue solvent-accessible surface areas (SASA) were computed using
350 GROMACS v2018.1, which utilizes the double cubic lattice method (DCLM) described by Eisenhaber et
351 al.[28] The change in solvent accessible area was computed as

352 $$\Delta SASA = SASA_{fragments} - SASA_{reconstituted}$$

353 where structures of the N and C-terminal fragments were isolated from the crystal structure.

354

355 **Computational Interface Scanning**

356 All modeling calculations were performed using the *Rosetta* molecular modeling suite v3.9. Single-point
357 mutants were generated using the standard Relax application, which enables local conformational sampling
358 to minimize energy (**Supplementary Note 1** includes full details). The total energy (ΔG_{Total}) of each mutant
359 was computed as the average of 100 relaxed models. The energy perturbation to total energy was
360 computed as

361 $$\Delta\Delta G_{Total} = \Delta G_{Total}^{Mutant} - \Delta G_{Total}^{WT}$$

362 The Rosetta Scripts application with the InterfaceAnalyzeMover was applied to each relaxed model to
363 compute the average residue-residue interaction energies between the N- and C-terminal fragments
364 (**Supplementary Note 1** includes the full details). The interfacial energy was computed as the pair-wise
365 sum of all short-range interaction energies as shown by

366 $$\Delta G_{Interfacial} = \sum_i \sum_j Energy_{i-j}^{SR}$$

367 where i and j denote the sets of residues within each fragment. The energy perturbation of each mutation
368 to the interfacial energy was then computed as

369 $$\Delta\Delta G_{Interfacial} = \Delta G_{Interfacial}^{Mutant} - \Delta G_{Interfacial}^{WT}$$

370

371 **Phenotype Classifier**

372 Experimentally characterized variants were assigned class labels (not-inducible, inducible and dead) based
373 on reporter expression levels in the ligand-absent and ligand-induced states. Variants with ≥1.2 fold higher
374 reporter expression in the ligand-induced state relative to the ligand-absent state were labeled as inducible.
375 For variants with expression levels <5% of wild-type (WT) sequence in the ligand-induced state and <1.2
376 fold activation were classified as functionally dead. The remaining variants were assigned the not-inducible
377 class label.
378
379 **STATISTICAL ANALYSIS**
380
381 Statistical details for each experiment are included the figure legends. The data shown reflect the mean
382 across these biological replicates of the mean fluorescence intensity (MFI) of approximately 2,000–3,000
383 single, transfected cells. Error bars represent the SEM (standard error of the mean). For statistical
384 analyses, two-tailed Student's t-tests were used to evaluate whether a significant difference exists between
385 two groups of samples, and the reported comparisons meet the two requirements of this test: (1) the values
386 compared are expected to be derived from a normal distribution, and (2) the variance of each group is
387 expected to be comparable to that of the comparison group since the same transfection methodologies and
388 data collection methods were used for all samples that were compared. A p value of ≤ 0.05 was considered
389 to be statistically significant.
390
391 **DATA AVAILABILITY**
392
393 Data reported in composite figures (**Figs. 2a,b,d**, **3a, 4b, Supplementary Fig. 4**) are included as **Source**
394 **Data**.
395
396 **CODE AVAILABILITY**
397
398 Rosetta details and script are provided in **Supplementary Note 1**.
399

ACKNOWLEDGEMENTS

This work was supported in part by the National Institute of Biomedical Imaging and Bioengineering of the NIH under Award Number 1R01EB026510 (JNL); the Northwestern University Flow Cytometry Core Facility supported by Cancer Center Support Grant (NCI 5P30CA060553); T.B.D was supported by the Department of Defense (DoD) through the National Defense Science & Engineering Graduate Fellowship (NDSEG). This work is also supported in part by the Great Lakes Bioenergy Research Center, U. S. Department of Energy, Office of Science, Office of Biological and Environmental Research under Award Number DE-SC0018409 (S.R and A.T.M). The content is solely the responsibility of the authors and does not necessarily represent the official views of the NIH, Department of Defense, Department of Energy or other federal agencies.

AUTHOR CONTRIBUTIONS

T.B.D., A.T.M., S.R, and J.N.L conceptualized the project. T.B.D., J.D.B, W.K.C., E.E.S, created reagents, designed and performed experiments, and analyzed the data. A.N.P. assisted in analyzing and visualizing the data. A.T.M., developed the computational model and code. T.B.D., A.T.M., S.R., and J.N.L. drafted the manuscript, T.B.D., A.T.M., and A.N.P. created the figures. J.N.L. and S.R. supervised the work. All authors edited and approved the final manuscript.

COMPETING INTERESTS

J.N.L is a co-inventor on a patent that covers the MESA technology used in this manuscript (US Patent 9,732,392 B2).

426 **REFERENCES**

427 1. Romei, M.G. & Boxer, S.G. Split Green Fluorescent Proteins: Scope, Limitations, and Outlook.
428 *Annual Review of Biophysics* **48**, 19-44 (2019).

429 2. Shekhawat, S.S. & Ghosh, I. Split-protein systems: beyond binary protein-protein interactions. *Curr*
430 *Opin Chem Biol* **15**, 789-797 (2011).

431 3. Wehr, M.C. & Rossner, M.J. Split protein biosensor assays in molecular pharmacological studies.
432 *Drug Discovery Today* **21**, 415-429 (2016).

433 4. Muller, J. & Johnsson, N. Split-ubiquitin and the split-protein sensors: chessman for the endgame.
434 *Chembiochem* **9**, 2029-2038 (2008).

435 5. Paulmurugan, R. & Gambhir, S.S. Monitoring protein-protein interactions using split synthetic
436 renilla luciferase protein-fragment-assisted complementation. *Anal Chem* **75**, 1584-1589 (2003).

437 6. Dixon, A.S. et al. NanoLuc Complementation Reporter Optimized for Accurate Measurement of
438 Protein Interactions in Cells. *ACS chemical biology* **11**, 400-408 (2016).

439 7. Ozawa, T., Kaihara, A., Sato, M., Tachihara, K. & Umezawa, Y. Split luciferase as an optical probe
440 for detecting protein-protein interactions in mammalian cells based on protein splicing. *Analytical*
441 *Chemistry* **73**, 2516-2521 (2001).

442 8. Gray, D.C., Mahrus, S. & Wells, J.A. Activation of specific apoptotic caspases with an engineered
443 small-molecule-activated protease. *Cell* **142**, 637-646 (2010).

444 9. Gao, X.J., Chong, L.S., Kim, M.S. & Elowitz, M.B. Programmable protein circuits in living cells.
445 *Science* **361**, 1252-1258 (2018).

446 10. Fink, T. et al. Design of fast proteolysis-based signaling and logic circuits in mammalian cells.
447 *Nature chemical biology* **15**, 115-122 (2019).

448 11. Zetsche, B., Volz, S.E. & Zhang, F. A split-Cas9 architecture for inducible genome editing and
449 transcription modulation. *Nature biotechnology* **33**, 139-142 (2015).

450 12. Nihongaki, Y., Otabe, T., Ueda, Y. & Sato, M. A split CRISPR–Cpf1 platform for inducible genome
451 editing and gene activation. *Nature chemical biology* **15**, 882-888 (2019).

452 13. Paulmurugan, R., Umezawa, Y. & Gambhir, S.S. Noninvasive imaging of protein-protein
453 interactions in living subjects by using reporter protein complementation and reconstitution
454 strategies. *Proc Natl Acad Sci U S A* **99**, 15608-15613 (2002).
455 14. Fetchko, M. & Stagljar, I. Application of the split-ubiquitin membrane yeast two-hybrid system to
456 investigate membrane protein interactions. *Methods* **32**, 349-362 (2004).
457 15. Pandey, N., Nobles, C.L., Zechiedrich, L., Maresso, A.W. & Silberg, J.J. Combining random gene
458 fission and rational gene fusion to discover near-infrared fluorescent protein fragments that report
459 on protein-protein interactions. *ACS Synth Biol* **4**, 615-624 (2015).
460 16. Jones, K.A. et al. Development of a Split Esterase for Protein–Protein Interaction-Dependent Small-
461 Molecule Activation. *ACS Central Science* (2019).
462 17. Wehr, M.C., Reinecke, L., Botvinnik, A. & Rossner, M.J. Analysis of transient phosphorylation-
463 dependent protein-protein interactions in living mammalian cells using split-TEV. *BMC Biotechnol*
464 **8**, 55 (2008).
465 18. Camacho-Soto, K., Castillo-Montoya, J., Tye, B. & Ghosh, I. Ligand-gated split-kinases. *J Am*
466 *Chem Soc* **136**, 3995-4002 (2014).
467 19. Camacho-Soto, K., Castillo-Montoya, J., Tye, B., Ogunleye, L.O. & Ghosh, I. Small molecule gated
468 split-tyrosine phosphatases and orthogonal split-tyrosine kinases. *J Am Chem Soc* **136**, 17078-
469 17086 (2014).
470 20. Fink, T. et al. Design of fast proteolysis-based signaling and logic circuits in mammalian cells. *Nat*
471 *Chem Biol* **15**, 115-122 (2019).
472 21. Daringer, N.M., Dudek, R.M., Schwarz, K.A. & Leonard, J.N. Modular extracellular sensor
473 architecture for engineering mammalian cell-based devices. *ACS Synth Biol* **3**, 892-902 (2014).
474 22. Wehr, M.C. et al. Monitoring regulated protein-protein interactions using split TEV. *Nature Methods*
475 **3**, 985-993 (2006).
476 23. Crescitelli, R. et al. Distinct RNA profiles in subpopulations of extracellular vesicles: apoptotic
477 bodies, microvesicles and exosomes. *J Extracell Vesicles* **2** (2013).
478 24. Kapust, R.B., Tozser, J., Copeland, T.D. & Waugh, D.S. The P1' specificity of tobacco etch virus
479 protease. *Biochem Biophys Res Commun* **294**, 949-955 (2002).

480 25. Hartfield, R.M., Schwarz, K.A., Muldoon, J.J., Bagheri, N. & Leonard, J.N. Multiplexing Engineered
481 Receptors for Multiparametric Evaluation of Environmental Ligands. *Acs Synthetic Biology* **6**, 2042-
482 2055 (2017).
483 26. Schwarz, K.A., Daringer, N.M., Dolberg, T.B. & Leonard, J.N. Rewiring human cellular input-output
484 using modular extracellular sensors. *Nat Chem Biol* **13**, 202-209 (2017).
485 27. Donahue, P.S., Draut, J.W., Muldoon, J.J., Edelstein, H.I., Bagheri, N., Leonard, J.N. COMET: A
486 toolkit for compsoing customizable genetic programs in mammalian cells. *bioRxiv* (2019).
487 28. Eisenhaber, F., Lijnzaad, P., Argos, P., Sander, C. & Scharf, M. The double cubic lattice method:
488 Efficient approaches to numerical integration of surface area and volume and to dot surface
489 contouring of molecular assemblies. *Journal of Computational Chemistry* **16**, 273-284 (1995).

490

491

492

493 **FIGURES**

494

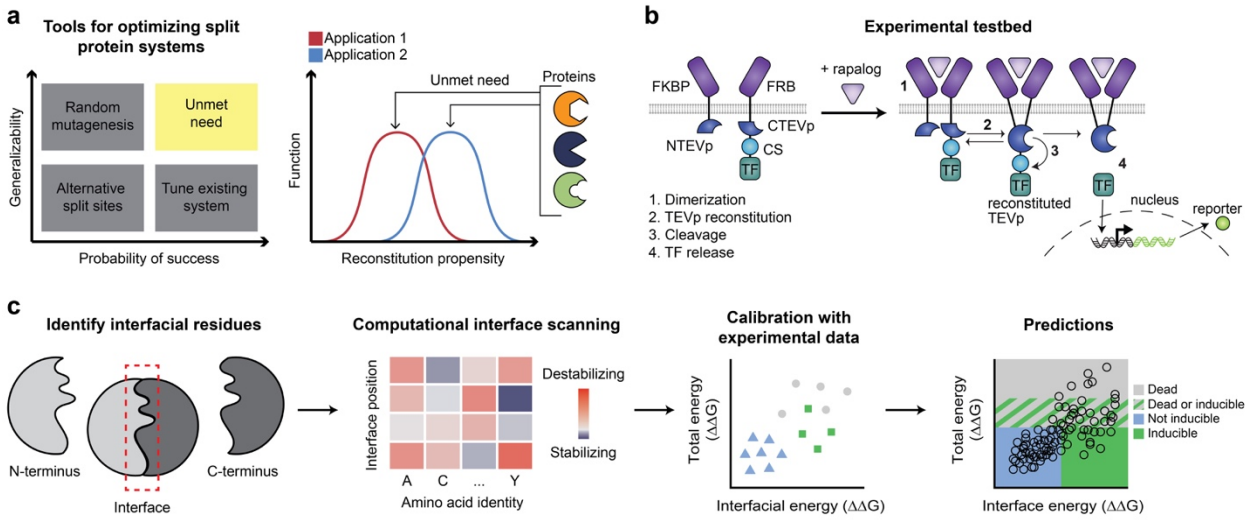

495

496 **Fig. 1 Design-driven strategy for tuning split protein systems. a,** Current methods for optimizing split
497 proteins are limited (left); an ideal tool would enable adapting split proteins for multiple applications, each
498 of which may require distinct reconstitution propensities (right). **b,** This cartoon illustrates the experimental
499 testbed used here; ligand binding-induced chain dimerization results in split TEVp reconstitution, trans-
500 cleavage, and release of a previously sequestered transcription factor to drive reporter expression. **c,** Split
501 Protein Optimization by Reconstitution Tuning (SPORT) workflow: identify important residues at the split
502 interface which are mutable, identify mutations that alter the total and interfacial energy, and use an
503 application-specific model, trained on limited experiments, to identify those mutations that are predicted to
504 yield a desired functional phenotype.

505

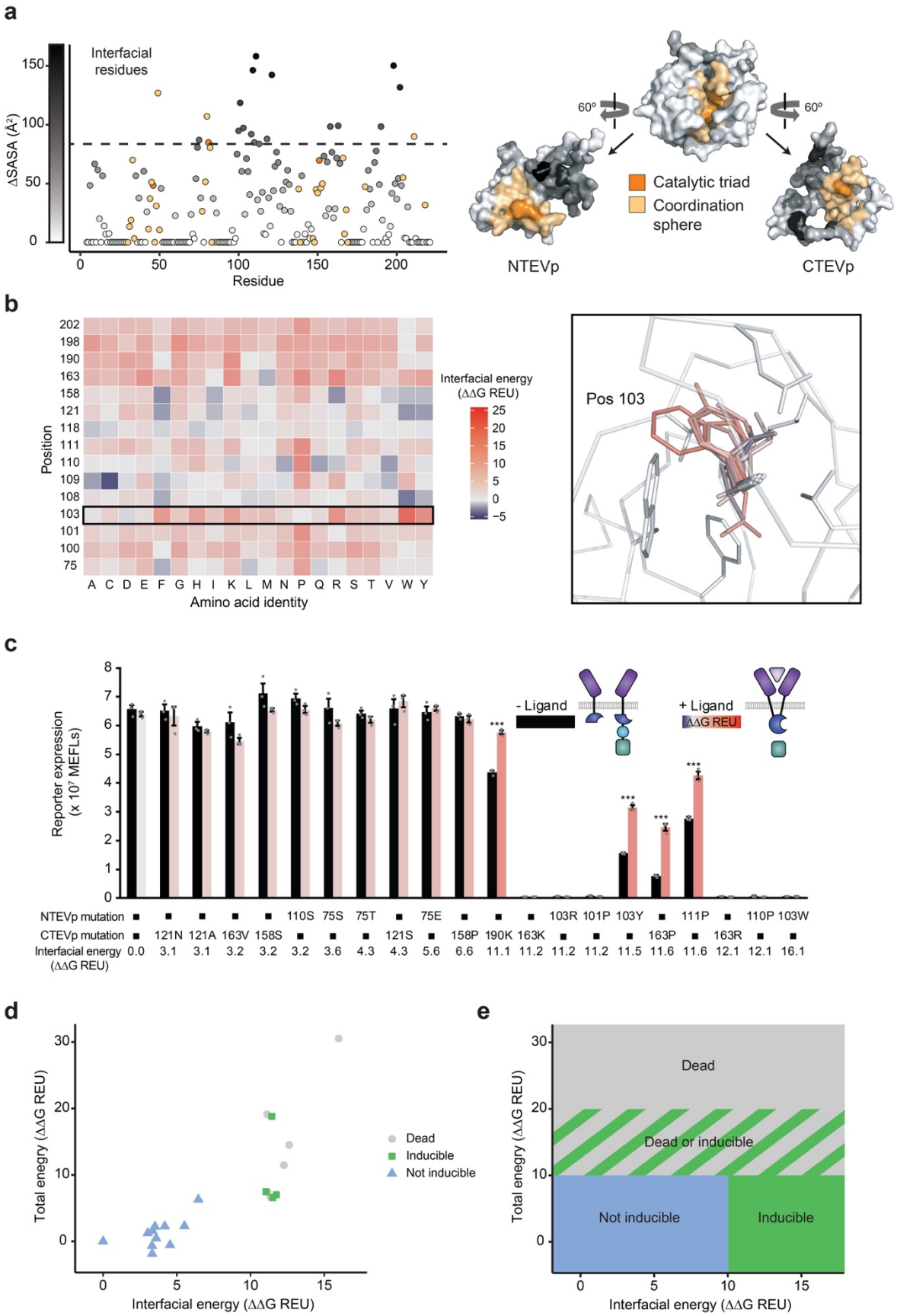
a
Interfacial residues
ΔSASA (Å²)
Residue
60°
60°
Catalytic triad
Coordination sphere
NTEVp
CTEVp
b
Position
Amino acid identity
Interfacial energy (ΔΔG REU)
Pos 103
c
Reporter expression (x 10⁷ MEFLs)
- Ligand
+ Ligand
ΔΔG REU
NTEVp mutation
CTEVp mutation
Interfacial energy (ΔΔG REU)
d
Total enegry (ΔΔG REU)
Interfacial energy (ΔΔG REU)
Dead
Inducible
Not inducible
e
Dead
Dead or inducible
Not inducible
Inducible

506

507 **Fig. 2 Computation guided method development and experimental analysis. a,** Left, characterization
508 of the solvent accessible surface area (SASA) of each residue of 118/119 split TEVp. Right, 3D depiction
509 of 118/119 split TEVp, showing the catalytic triad (orange), coordination sphere (yellow), and ΔSASA
510 (greyscale). **b,** Mutational scanning of high ΔSASA residues (left) and example of all possible mutations of
511 residue 103 (right), with change in interfacial energy indicated by color. **c,** Experimental analysis of TEVp
512 mutations predicted to span a range of interfacial energies. Error bars depict S.E.M. (*$p \leq 0.05$, ***$p \leq$
513 0.001). **d,** Experimental phenotypes observed in **c** were plotted on an energy landscape and annotated as
514 indicated by color (reporter expression normalized to WT < 0.05 is "dead", fold induction < 1.2 is "not
515 inducible", fold induction ≥ 1.2 is "inducible"). **e,** Proposed model for predicting zones of functional
516 phenotypes based upon total and interfacial energy; the boundaries were proposed based upon
517 observations using the initial 20 mutants tested in **c**.
518

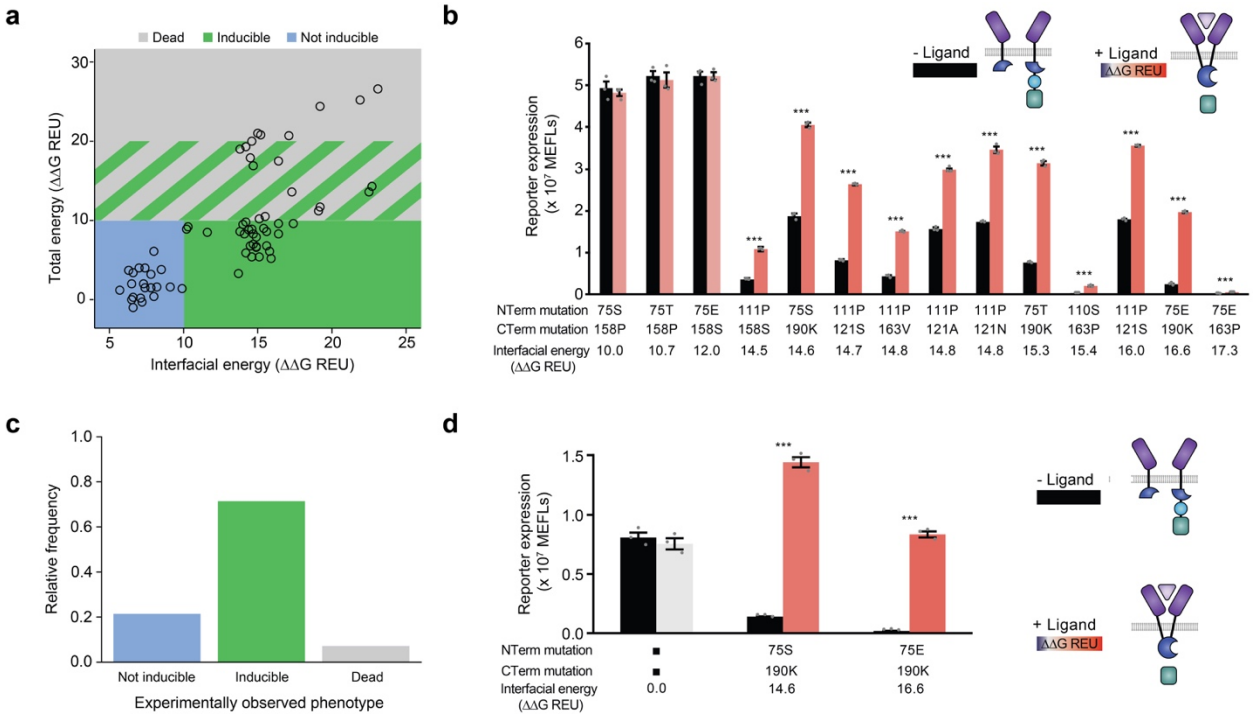

Fig. 3 Evaluation of model-predicted phenotypes for combined mutations. a, Computed energies and predicted phenotypes based on the classifier model—proposed in **Fig. 2e**—of all possible double and paired mutants constructed by combinatorial sampling of the initial single mutants tested (omitting dead mutations) in **Fig. 2c**. **b,** Experimental evaluation of selected mutants predicted to be inducible. **c,** Experimentally observed phenotypes for the fourteen mutants predicted to be inducible (from **b**), showing that the model predicts inducibility at a fairly high rate (10/14). **d,** Normalizing protein expression levels improves performance (fold induction) of selected mutants (from **b**), whereas WT function is not changed. Normalization was achieved using Western Blot analysis (**Supplementary Fig. L4)** to adjust DNA doses transfected (per well, N-terminal chains: 0.4 ng WT, 1 ng 75S, 1.4 ng 75E; C-terminal chains: 5 ng WT, 12 ng 190K). Error bars depict S.E.M. (*$p \leq 0.05$, ***$p \leq 0.001$).

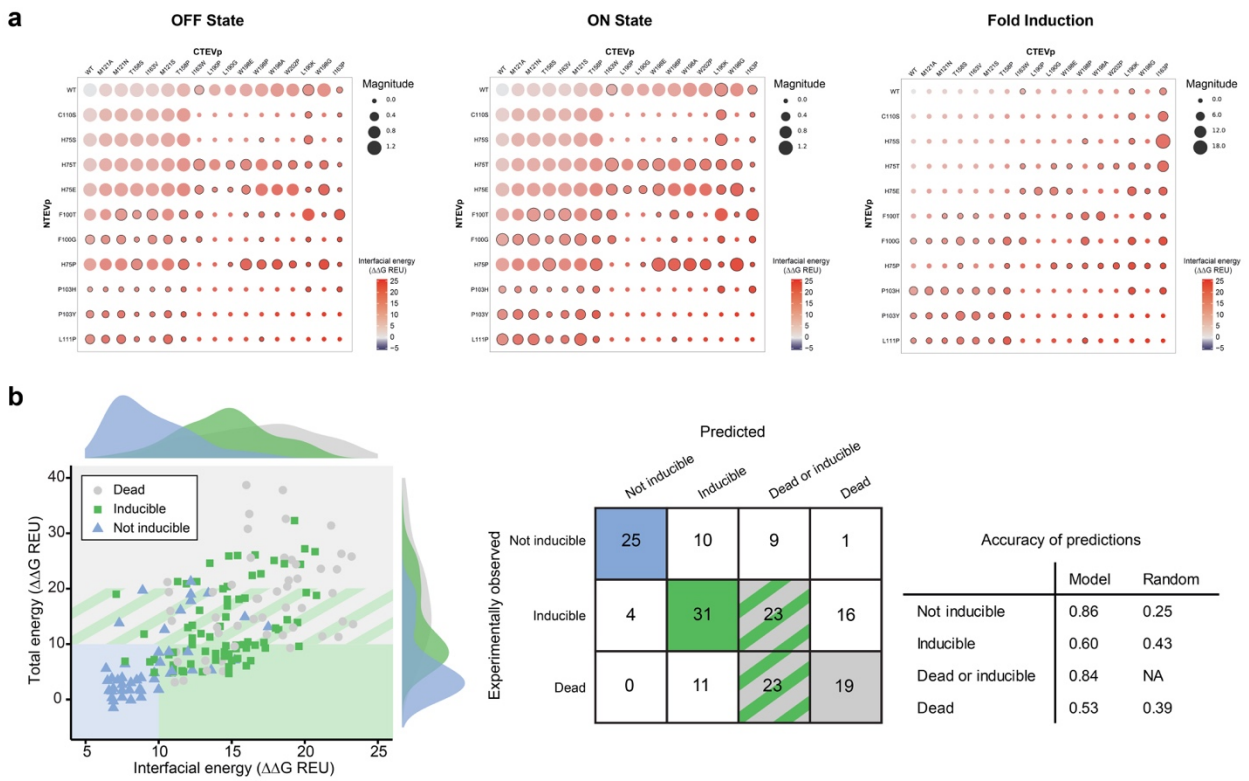

Fig. 4 Evaluation of model-predicted phenotypes for novel mutations and combinations. a, For each experimentally characterized construct, reporter output was quantified in the absence of ligand (OFF state) and following ligand addition (ON state), and the fold induction was calculated. Calculated interfacial energy for each construct is indicated by circle *color*, magnitude of reporter expression (or fold-induction) is indicated by circle *size*, and constructs with a fold induction ≥ 1.2 are denoted with a black border. Single mutants observed to be dead (**Fig. 2**) were not carried forward to this analysis. **b,** Left, experimentally observed phenotypes (data point color) were mapped onto the proposed classifier model from **Fig. 2e**, with observed frequency distributions shown as histograms. Right, evaluation of model prediction accuracy compared to random assignment of phenotypes.

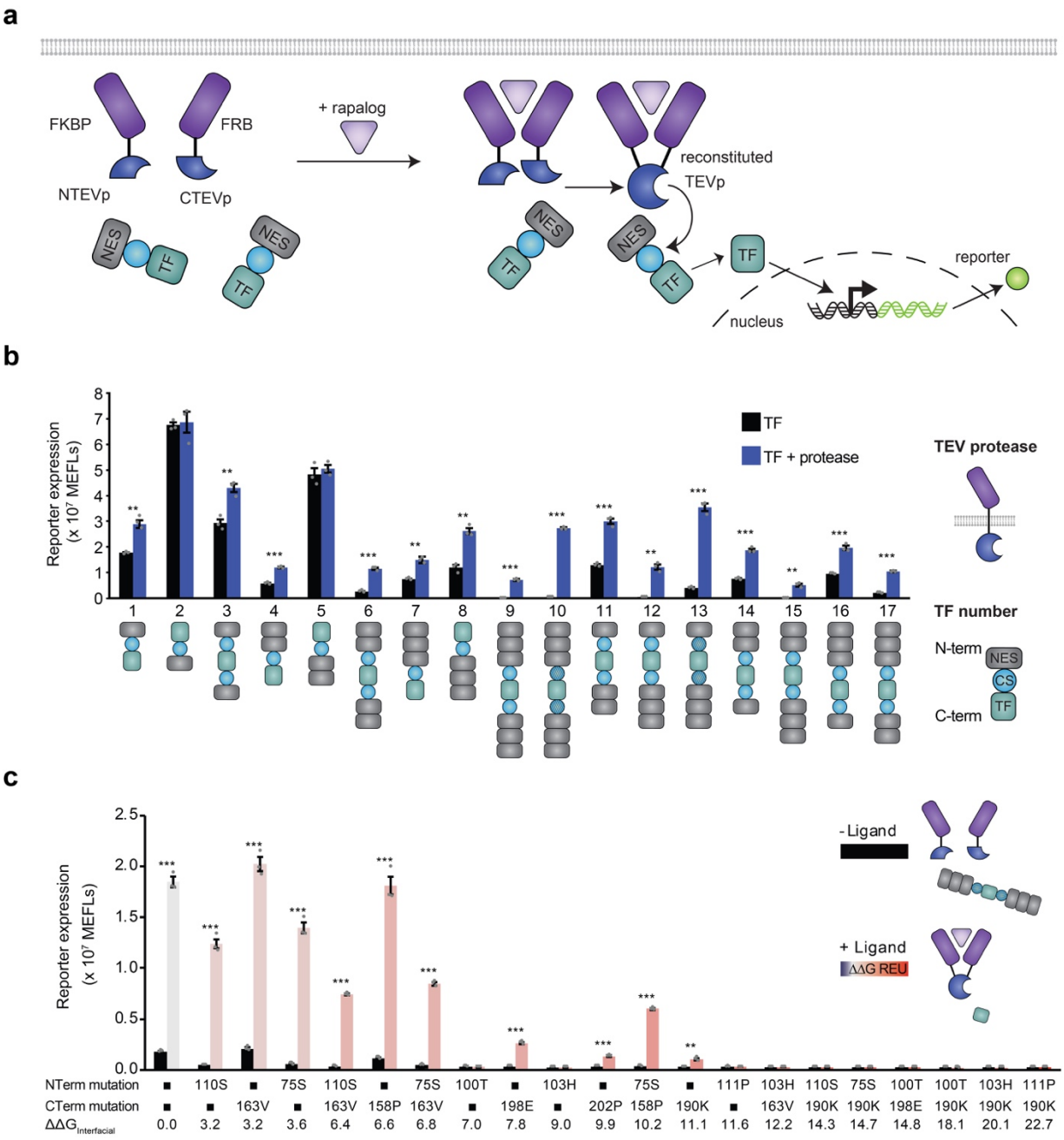

Fig. 5 Model guided design of a new split TEVp application in soluble context. a, This cartoon illustrates the soluble split TEVp testbed. Ligand-binding-induced dimerization mediates reconstitution of split TEVp, which then cleaves one or more nuclear export sequence (NES) elements from a soluble transcription factor, leading to nuclear import and reporter expression. **b,** Developing the testbed by evaluating engineered transcription factors (TF) for consistency with the mechanism proposed in **a**; shaded cleavage sequence (CS) domains indicate a G residue in the P1' position, unshaded CS domains indicate

549 a M residue in this position.[24] **c,** Experimental analysis of single and paired mutants sampling a range of
550 interfacial energies (indicated by color and labeled), employing TF10 from **b**. Error bars depict S.E.M. (*$p \leq$
551 0.05, ***$p \leq 0.001$).
552

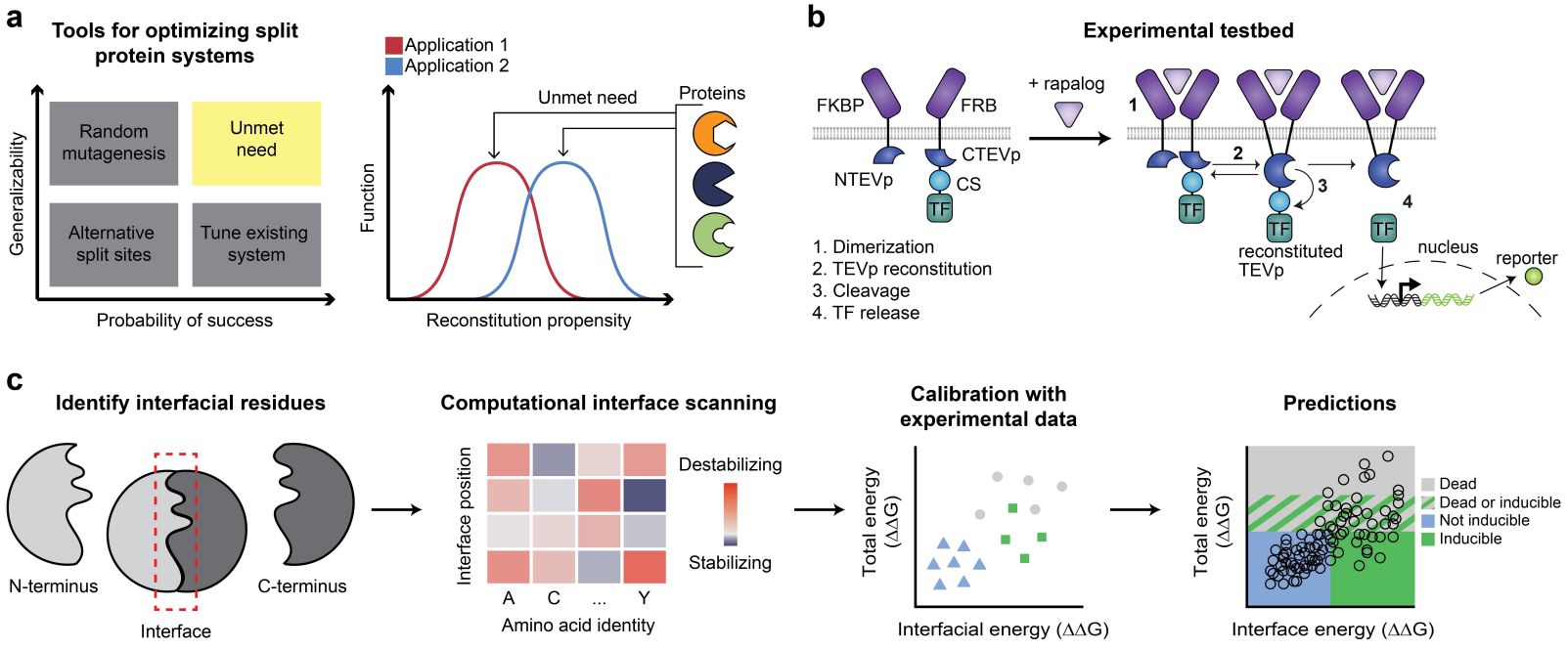
a
Tools for optimizing split protein systems
Generalizability
Random mutagenesis
Unmet need
Alternative split sites
Tune existing system
Probability of success
Application 1
Application 2
Unmet need
Proteins
Function
Reconstitution propensity
b
Experimental testbed
FKBP
FRB
+ rapalog
NTEVp
CTEVp
CS
TF
1. Dimerization
2. TEVp reconstitution
3. Cleavage
4. TF release
reconstituted TEVp
nucleus
reporter
c
Identify interfacial residues
N-terminus
C-terminus
Interface
Computational interface scanning
Interface position
Destabilizing
Stabilizing
A
C
...
Y
Amino acid identity
Calibration with experimental data
Total energy (ΔΔG)
Interfacial energy (ΔΔG)
Predictions
Total energy (ΔΔG)
Dead
Dead or inducible
Not inducible
Inducible
Interface energy (ΔΔG)

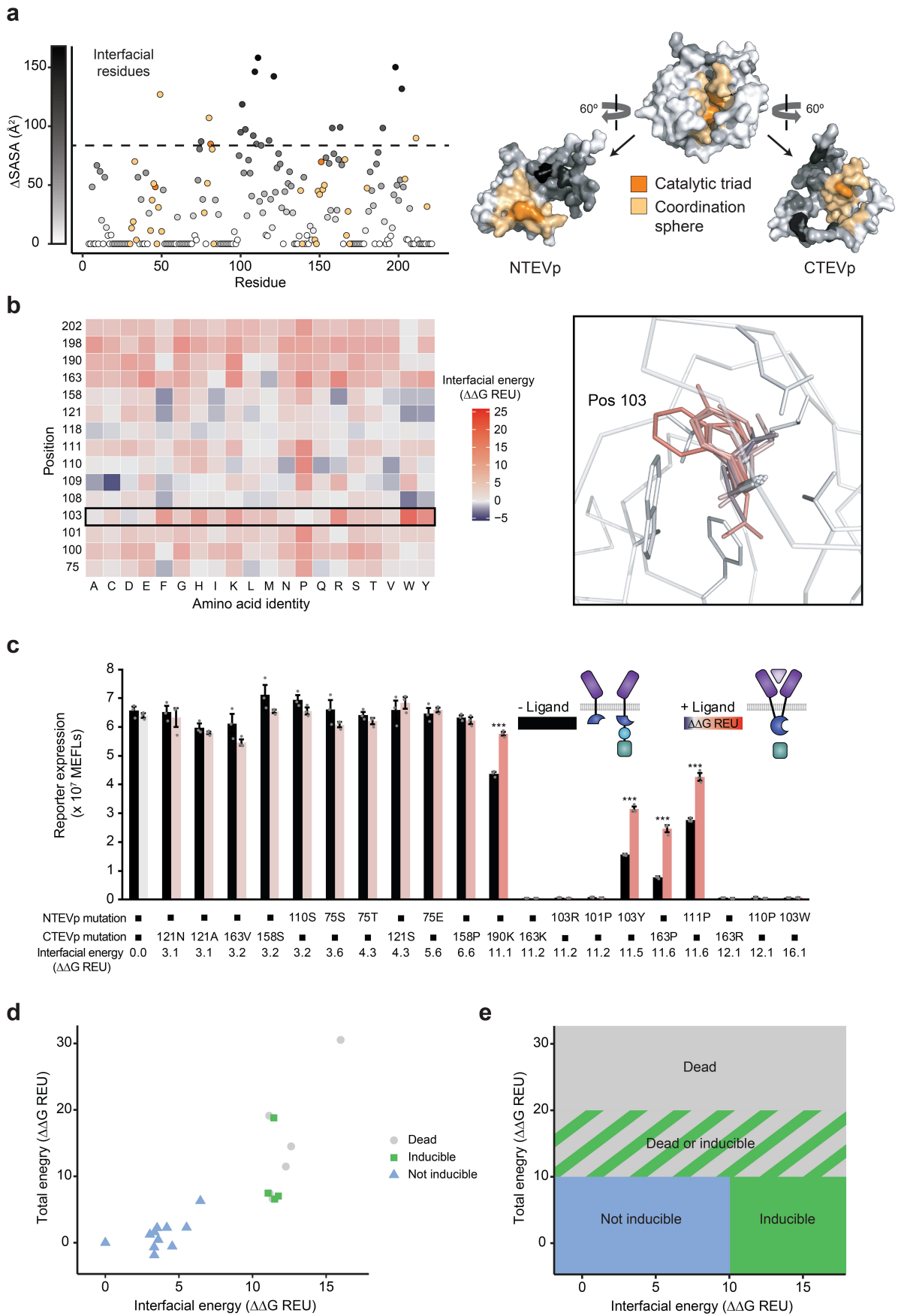
a
Interfacial residues
ΔSASA (Å²)
150
100
50
0
0
50
100
150
200
Residue
60º
60º
Catalytic triad
Coordination sphere
NTEVp
CTEVp
b
Position
202
198
190
163
158
121
118
111
110
109
108
103
101
100
75
A C D E F G H I K L M N P Q R S T V W Y
Amino acid identity
Interfacial energy (ΔΔG REU)
25
20
15
10
5
0
−5
Pos 103
c
Reporter expression (x 10⁷ MEFLs)
8
7
6
5
4
3
2
1
0
- Ligand
+ Ligand
ΔΔG REU
***
NTEVp mutation
CTEVp mutation
Interfacial energy (ΔΔG REU)
NTEVp mutation: 110S 75S 75T 75E 103R 101P 103Y 111P 110P 103W
CTEVp mutation: 121N 121A 163V 158S 121S 158P 190K 163K 163P 163R
Interfacial energy (ΔΔG REU): 0.0 3.1 3.1 3.2 3.2 3.2 3.6 4.3 4.3 5.6 6.6 11.1 11.2 11.2 11.2 11.5 11.6 11.6 12.1 12.1 16.1
d
Total enegry (ΔΔG REU)
30
20
10
0
0
5
10
15
Interfacial energy (ΔΔG REU)
Dead
Inducible
Not inducible
e
Total enegry (ΔΔG REU)
30
20
10
0
Dead
Dead or inducible
Not inducible
Inducible
0
5
10
15
Interfacial energy (ΔΔG REU)

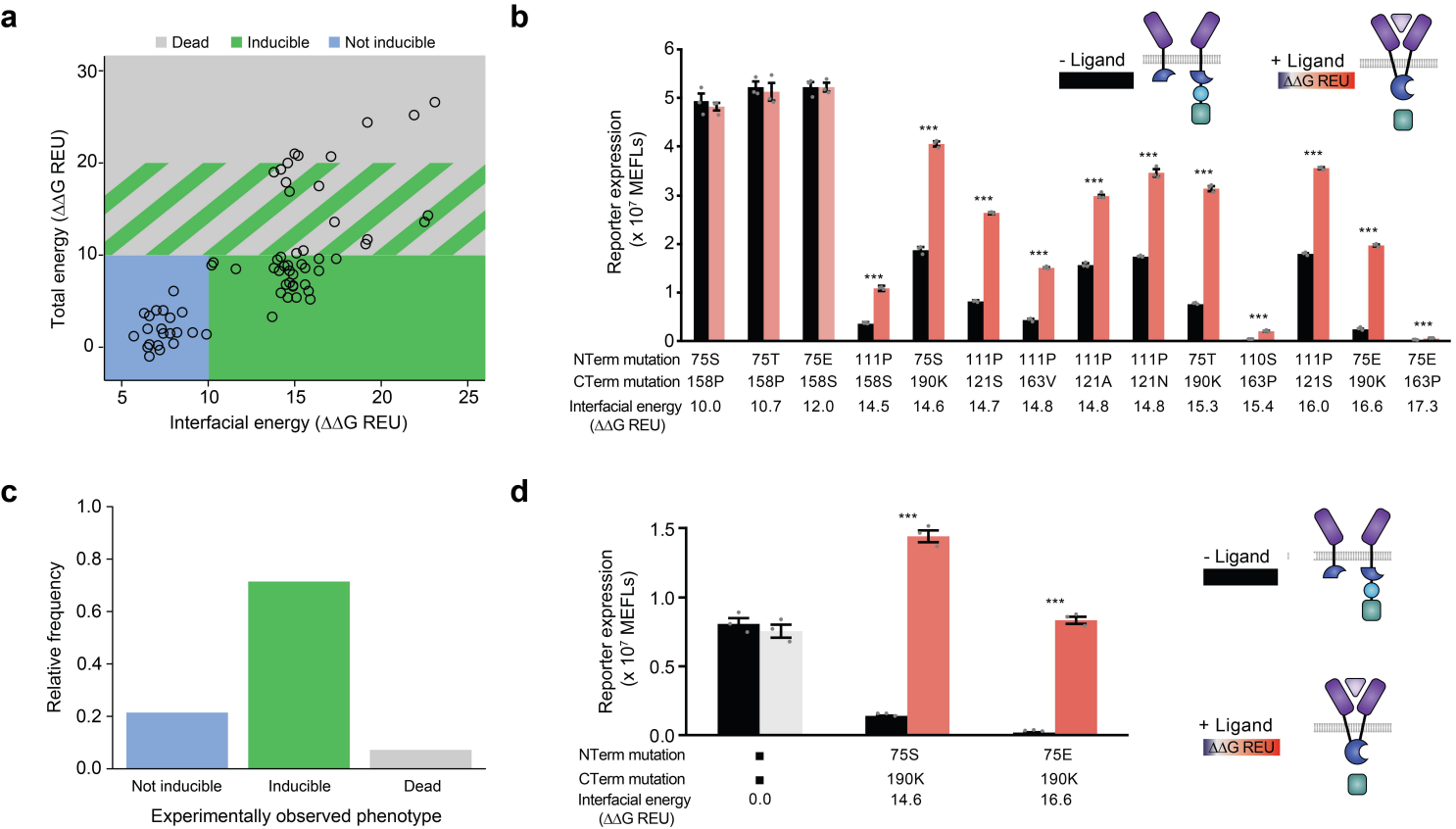
a
Dead
Inducible
Not inducible
Total energy (ΔΔG REU)
Interfacial energy (ΔΔG REU)
b
- Ligand
+ Ligand
ΔΔG REU
Reporter expression (x 10⁷ MEFLs)
NTerm mutation 75S 75T 75E 111P 75S 111P 111P 111P 111P 75T 110S 111P 75E 75E
CTerm mutation 158P 158P 158S 158S 190K 121S 163V 121A 121N 190K 163P 121S 190K 163P
Interfacial energy (ΔΔG REU) 10.0 10.7 12.0 14.5 14.6 14.7 14.8 14.8 14.8 15.3 15.4 16.0 16.6 17.3
c
Relative frequency
Not inducible
Inducible
Dead
Experimentally observed phenotype
d
Reporter expression (x 10⁷ MEFLs)
NTerm mutation 75S 75E
CTerm mutation 190K 190K
Interfacial energy (ΔΔG REU) 0.0 14.6 16.6
- Ligand
+ Ligand
ΔΔG REU

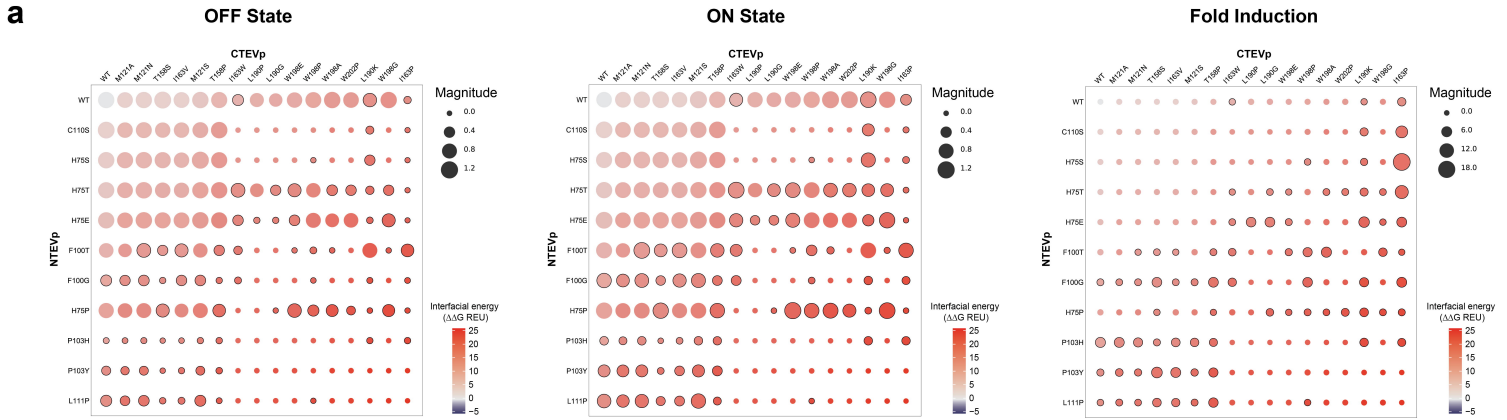

b

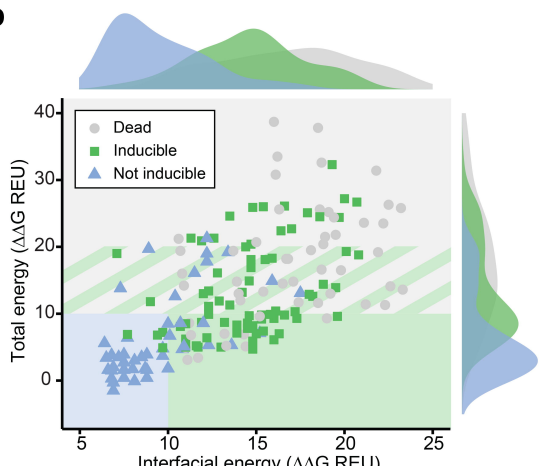

Predicted

Experimentally observed	Not inducible	Inducible	Dead or inducible	Dead
Not inducible	25	10	9	1
Inducible	4	31	23	16
Dead	0	11	23	19

Accuracy of predictions

	Model	Random
Not inducible	0.86	0.25
Inducible	0.60	0.43
Dead or inducible	0.84	NA
Dead	0.53	0.39

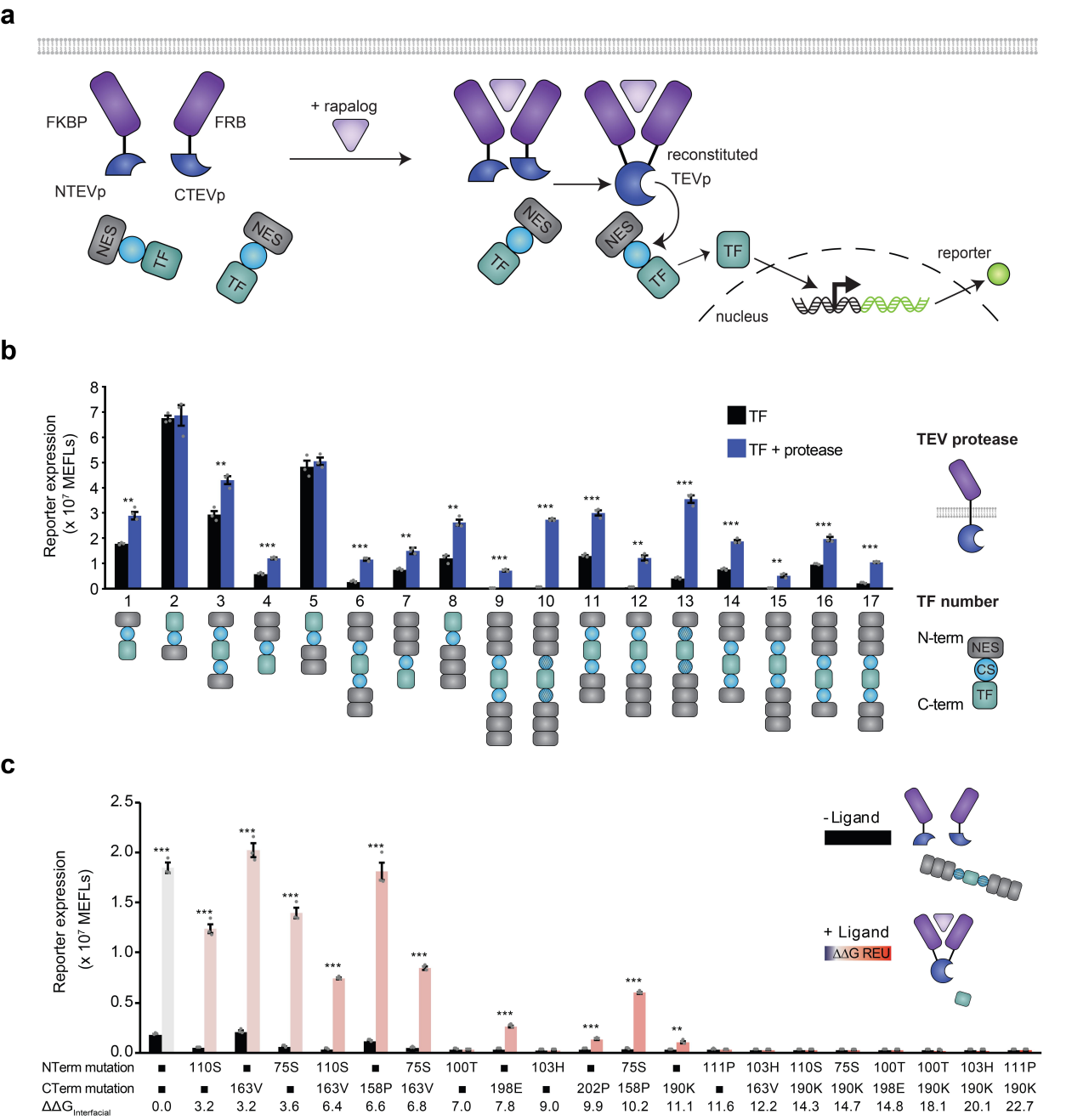
a
FKBP
FRB
NTEVp
CTEVp
+ rapalog
reconstituted
TEVp
NES
TF
nucleus
reporter
b
Reporter expression
(x 10^7 MEFLs)
TF
TF + protease
TEV protease
TF number
N-term
C-term
CS
c
Reporter expression
(x 10^7 MEFLs)
- Ligand
+ Ligand
ΔΔG REU
NTerm mutation
CTerm mutation
ΔΔG Interfacial
0.0 3.2 3.2 3.6 6.4 6.6 6.8 7.0 7.8 9.0 9.9 10.2 11.1 11.6 12.2 14.3 14.7 14.8 18.1 20.1 22.7